Check for updates

RESEARCH ARTICLE

ADVANCED FUNCTIONAL MATERIALS
www.afm-journal.de

Low-Dielectric and Submicron-Resolution Photosensitive Polyimide Substrate for Large-Scale Pattern Customization and Low-Signal-Loss Transmission with Nanotesla-Scale Quantum Sensing Potential

Zhiyuan Peng, An Ye, Yubin Pu, Yutong Tang, Ling Zhang, Yueping Niu,* and Chunzhong Li**

Photosensitive polyimide (PSPI) integrates photoresist and dielectric interlayer functions for efficient electronic fabrication, yet suffers from limited resolution and elevated dielectric constants, particularly in advanced integrated circuits (ICs). In this study, through integrated molecular design and component screening, a novel PSPI system incorporating intrinsically low-polarization photosensitive groups and efficient chemical amplification is found to exhibit low dielectric properties ($\varepsilon = 2.241$, $\tan\delta = 0.0137$ at 10 GHz), submicron-level resolution (≈880 nm), low thermal imidization temperature (180°C), and low coefficient of thermal expansion (26 ppm K^{-1}). This PSPI system is fully compatible with modern IC manufacturing processes, and its superior photosensitivity (33.15 mJ cm^{-2}) and high contrast (3.03) further support laser direct writing. Moreover, as an encapsulation material and dielectric interlayer in flexible multilayer circuits, the PSPI system demonstrates robust bending durability and enhances high-frequency signal integrity with minimal parasitic capacitance. Coupled with nanodiamond nitrogen-vacancy centers, low-dielectric PSPI-based circuit boards significantly improve quantum sensing and imaging, providing higher signal fidelity and enabling precise nanotesla-scale measurements in weak magnetic fields. This breakthrough advances the resolution of PSPI to an unprecedented nanometer scale while maintaining exceptional dielectric performance, establishing it as a pivotal enabler for next-generation flexible integrated systems requiring precise signal transmission.

1. Introduction

Conventional interlayer dielectric polymers require the application of an additional photoresist layer on the dielectric surface when patterning is necessary, and the final pattern is produced via a multi-step sequence of photoresist exposure and development, dielectric layer etching, and photoresist removal.[1] In contrast, photosensitive polyimides (PSPIs) combine the roles of both the dielectric interlayer and photoresist due to their insulating properties and patterning abilities, requiring only exposure, development, and curing. This significantly enhances the manufacturing efficiency in integrated circuit production, while avoiding degradation in pattern clarity and contrast due to photoresist residues.[2] PSPIs offer the advantages of cost-effective, large-scale fabrication and meet the demanding requirements of high-performance electrical and electronic devices, with widespread applications in field-effect transistors,[3] photovoltaic memory,[4] imaging sensors,[5] and wafer-level chip packaging.[6] However, as electronics evolve toward high-frequency operation and high-wiring density,[7] PSPIs face significant challenges in achieving low dielectric constants ($\varepsilon < 2.5$ at 10 GHz)[8] and submicron-level resolution (<1 µm),[9] which are essential for miniaturized designs, high-density interconnects, low-loss signal transmission, and enhanced computational performance in ICs.[10]

Currently, intrinsic PSPIs, developed by incorporating chromophores or modifying the polymer backbone to facilitate direct photoactivation,[11] possess excellent fundamental properties owing to their chemically uniform structure, good mechanical properties, and relatively low dielectric properties (low dielectric constants and loss). However, they typically suffer from low resolution and require high exposure doses. Choi et al. reported an intrinsic PSPI with a dielectric constant of 2.72, obtained by grafting hydroxylated polyimide with acryloyl chloride, but the material demonstrated a limited resolution (8 µm) and poor photosensitivity, necessitating a high exposure dose of 500 mJ cm^{-2}, which was unsuitable for precision micro/nanoscale processing.[12]

Z. Peng, Y. Pu, L. Zhang, C. Li
Key Laboratory for Ultrafine Materials of Ministry of Education
Shanghai Engineering Research Center of Hierarchical Nanomaterials
Frontiers Science Center for Materiobiology and Dynamic Chemistry
School of Materials Science and Engineering
East China University of Science and Technology
Shanghai 200237, P. R. China
E-mail: zlingzi@ecust.edu.cn; czli@ecust.edu.cn
A. Ye, Y. Tang, Y. Niu
School of Physics
East China University of Science and Technology
Shanghai 200237, P. R. China
E-mail: niuyp@ecust.edu.cn
Y. Pu
College of Polymer Science and Engineering
Sichuan University
Chengdu 610065, P. R. China
The ORCID identification number(s) for the author(s) of this article can be found under https://doi.org/10.1002/adfm.202509278

DOI: 10.1002/adfm.202509278

 © 2025 Wiley-VCH GmbH

Check for updates

ADVANCED FUNCTIONAL MATERIALS
www.afm-journal.de

Low-Dielectric and Submicron-Resolution Photosensitive Polyimide Substrate for Large-Scale Pattern Customization and Low-Signal-Loss Transmission with Nanotesla-Scale Quantum Sensing Potential

Zhiyuan Peng, An Ye, Yubin Pu, Yutong Tang, Ling Zhang, Yueping Niu,* and Chunzhong Li**

Photosensitive polyimide (PSPI) integrates photoresist and dielectric interlayer functions for efficient electronic fabrication, yet suffers from limited resolution and elevated dielectric constants, particularly in advanced integrated circuits (ICs). In this study, through integrated molecular design and component screening, a novel PSPI system incorporating intrinsically low-polarization photosensitive groups and efficient chemical amplification is found to exhibit low dielectric properties ($\varepsilon = 2.241$, $\tan\delta = 0.0137$ at 10 GHz), submicron-level resolution (≈880 nm), low thermal imidization temperature (180°C), and low coefficient of thermal expansion (26 ppm K^{-1}). This PSPI system is fully compatible with modern IC manufacturing processes, and its superior photosensitivity (33.15 mJ cm^{-2}) and high contrast (3.03) further support laser direct writing. Moreover, as an encapsulation material and dielectric interlayer in flexible multilayer circuits, the PSPI system demonstrates robust bending durability and enhances high-frequency signal integrity with minimal parasitic capacitance. Coupled with nanodiamond nitrogen-vacancy centers, low-dielectric PSPI-based circuit boards significantly improve quantum sensing and imaging, providing higher signal fidelity and enabling precise nanotesla-scale measurements in weak magnetic fields. This breakthrough advances the resolution of PSPI to an unprecedented nanometer scale while maintaining exceptional dielectric performance, establishing it as a pivotal enabler for next-generation flexible integrated systems requiring precise signal transmission.

1. Introduction

Conventional interlayer dielectric polymers require the application of an additional photoresist layer on the dielectric surface when patterning is necessary, and the final pattern is produced via a multi-step sequence of photoresist exposure and development, dielectric layer etching, and photoresist removal.[1] In contrast, photosensitive polyimides (PSPIs) combine the roles of both the dielectric interlayer and photoresist due to their insulating properties and patterning abilities, requiring only exposure, development, and curing. This significantly enhances the manufacturing efficiency in integrated circuit production, while avoiding degradation in pattern clarity and contrast due to photoresist residues.[2] PSPIs offer the advantages of cost-effective, large-scale fabrication and meet the demanding requirements of high-performance electrical and electronic devices, with widespread applications in field-effect transistors,[3] photovoltaic memory,[4] imaging sensors,[5] and wafer-level chip packaging.[6] However, as electronics evolve toward high-frequency operation and high-wiring density,[7] PSPIs face significant challenges in achieving low dielectric constants ($\varepsilon < 2.5$ at 10 GHz)[8] and submicron-level resolution (<1 μm),[9] which are essential for miniaturized designs, high-density interconnects, low-loss signal transmission, and enhanced computational performance in ICs.[10]

Currently, intrinsic PSPIs, developed by incorporating chromophores or modifying the polymer backbone to facilitate direct photoactivation,[11] possess excellent fundamental properties owing to their chemically uniform structure, good mechanical properties, and relatively low dielectric properties (low dielectric constants and loss). However, they typically suffer from low resolution and require high exposure doses. Choi et al. reported an intrinsic PSPI with a dielectric constant of 2.72, obtained by grafting hydroxylated polyimide with acryloyl chloride, but the material demonstrated a limited resolution (8 μm) and poor photosensitivity, necessitating a high exposure dose of 500 mJ cm^{-2}, which was unsuitable for precision micro/nanoscale processing.[12]

Z. Peng, Y. Pu, L. Zhang, C. Li
Key Laboratory for Ultrafine Materials of Ministry of Education
Shanghai Engineering Research Center of Hierarchical Nanomaterials
Frontiers Science Center for Materiobiology and Dynamic Chemistry
School of Materials Science and Engineering
East China University of Science and Technology
Shanghai 200237, P. R. China
E-mail: zlingzi@ecust.edu.cn; czli@ecust.edu.cn

A. Ye, Y. Tang, Y. Niu
School of Physics
East China University of Science and Technology
Shanghai 200237, P. R. China
E-mail: niuyp@ecust.edu.cn

Y. Pu
College of Polymer Science and Engineering
Sichuan University
Chengdu 610065, P. R. China

The ORCID identification number(s) for the author(s) of this article can be found under https://doi.org/10.1002/adfm.202509278

DOI: 10.1002/adfm.202509278

 © 2025 Wiley-VCH GmbH

In contrast, chemically amplified PSPIs, typically composed of external crosslinking agents and photoactive catalysts, broaden the structural design flexibility of polyimides and enhance both resolution and photosensitivity. However, high additive concentrations can significantly increase the dielectric constant. Tseng et al. developed a polyamide acid solution containing 15 wt.% of a photo-base generator that decomposes into both a curing agent and an imidization catalyst, achieving a resolution of 4 µm but exhibiting a high dielectric constant of 3.8, thus compromising signal stability and transmission integrity.[13] Therefore, achieving a PSPI system that simultaneously exhibits a low dielectric constant and high resolution remains a significant and ongoing challenge.

According to the Rayleigh criterion and the numerical aperture of an optical system, lithography systems employing a 365 nm (i-line) illumination source can theoretically achieve sub-500 nm resolution capabilities. However, there are only a few reports of PSPIs achieving resolutions below 2 µm. High-resolution photosensitive polymers require uniform component dispersion, efficient UV absorption, and rapid crosslinking or decomposition reactions,[14] while also ensuring sharp pattern edges, high imaging contrast, and robust dimensional fidelity during photolithography.[15] Numerous studies have engineered PSPI with reduced molecular weights through chain end-capping strategies, effectively mitigating photoactive compound diffusion and enhancing the localization of crosslinking reactions. This approach improves pattern edge fidelity with respect to the original photomask geometry after exposure.[16] However, excessively low molecular weights of PSPI precursors can induce significant shrinkage during high-temperature cyclodehydration (usually 250–300 °C), particularly in fine-featured structures, where anisotropic stress accumulation can severely degrade pattern integrity.[17] In addition, high concentrations of photoactive additives or inorganic nanomaterials (e.g., quantum dots) are often incorporated to enhance the photosensitivity of PSPI; however, this approach also introduces optical scattering, which reduces pattern fidelity through edge acuity reduction.[18] Hence, attaining submicron-scale patterning in PSPI lithography necessitates synergistic optimization of curing temperature and effective photoinitiator systems at low additive concentrations.

In this study, an innovative PSPI system is developed by integrating intrinsic photosensitive groups and chemical amplification, which efficiently triggers the polymerization of low-polarization-rate photosensitive side groups at low organic photosensitizer concentrations (3 wt.%). This system achieves remarkably low dielectric constants, submicron-level resolution, and enhanced photosensitivity at reduced thermal imidization temperatures. Furthermore, the PSPI system is compatible with maskless lithography for large-scale pattern customization and field-effect transistor fabrication, aligning with the process requirements of modern high-density integrated circuits. It could also function as a dielectric interlayer and be encapsulated in multilayer circuit boards, offering excellent comprehensive performance and stable signal transmission capabilities. These attributes will contribute to the advancement of quantum metrology technologies, enabling weak, high-frequency signal transmission with enhanced accuracy and imaging resolution.

2. Results and Discussion

2.1. Synthesis and Screening of the PSPI System

The patterning principle of a PSPI system is based on the difference in solubility arising from the transformation into a crosslinked structure after UV exposure illustrated in **Figure 1a**. The PSPI precursor, poly(amide ester) (PAE), is synthesized through the isomerization of polyamide acid (PAA) followed by ring-opening reactions with vinyl-containing monomers (Figure S1, Supporting Information). This process enables the covalent grafting of photoreactive groups onto the side chains of polyisoimide (PII), thereby achieving photosensitive functionalization of the polymer structure. Fourier-transform infrared (FTIR) spectra confirm the successful synthesis of the product at each stage, as illustrated in Figure 1b. The peak at 921 cm^{-1} is attributed to the lactone ring of the exocyclic double bond in PII.[16d] Additionally, the disappearance of the N–H (3010 cm^{-1}) and O–H (2927 cm^{-1}) stretching bands indicated the nearly complete conversion of PAA to PII. The characteristic peaks observed at 3082 cm^{-1} (═C—H stretching), 1624 cm^{-1} (C═C stretching), and 1410 cm^{-1} (C—H bending) demonstrate the grafting of photosensitive groups onto the PAE. The PAE can be thermally imidized at 180 °C to form PSPI, lower than the ≈250 °C required for the direct PAA-to-PI conversion.[19] The absence of the characteristic double bond peaks at 3082 and 1624 cm^{-1} validates the formation of the crosslinked PSPI structure.[20]

The configuration of the polyimide (PI) backbone and photo-crosslinked chain segments plays a critical role in achieving both low dielectric constants and high-resolution patterning. The trifluoromethyl substituent (-CF_3) on the main chain introduces steric hindrance and strong electrophilicity, suppressing intermolecular charge-transfer complexation and decreasing molecular polarization.[21] Also, its pronounced electron-withdrawing effect renders adjacent photosensitive groups more electron-deficient, enhancing radical reactivity and accelerating photopolymerization.[22] Among the four investigated photosensitive variants (structural verification provided in Figure S2, Supporting Information ^{1}H-NMR spectra), the 2-hydroxyethyl acrylate (HEA)-grafted PSPI repeating unit exhibits the lowest volumetric dipole moment and polarizability (Table S1, Supporting Information), strategically contributing to the low dielectric constant of the final PSPI composite.

Three organic photoactive additives –MK (hydrogen abstraction), OXE-01 (bond cleavage), and i907 (homolysis) – are strategically selected for their absorption spectra within the shared near-UV range (300–400 nm) and distinct photochemical mechanisms (Figure S3, Supporting Information). The PSPI is formulated with 3 wt.% photoactive additives in PAE/dimethylacetamide (DMAc) solution after exposure and baking (FTIR of all PSPI composites are shown in Figure S4, Supporting Information). As elucidated in Figure 1c, the MK/PAE solution displays a strong absorption band at 355 nm, matching the emission of the maskless laser direct writing (LDW) system, and peaks at 365 nm, corresponding to the standard i-line wavelength used in the typical mask-aligner lithography. MK functions dually as a sensitizer[23] and a photoinitiator,[24] as well as synergistic interactions with the fluorinated PSPI backbone (see Note S1 and

© 2025 Wiley-VCH GmbH

16163028, 0, Downloaded from https://advanced.onlinelibrary.wiley.com/doi/10.1002/adfm.202509278 by Zhiyuan Peng - East China Uni Of Sci & Tech , Wiley Online Library on [27/06/2025]. See the Terms and Conditions (https://onlinelibrary.wiley.com/terms-and-conditions) on Wiley Online Library for rules of use; OA articles are governed by the applicable Creative Commons License

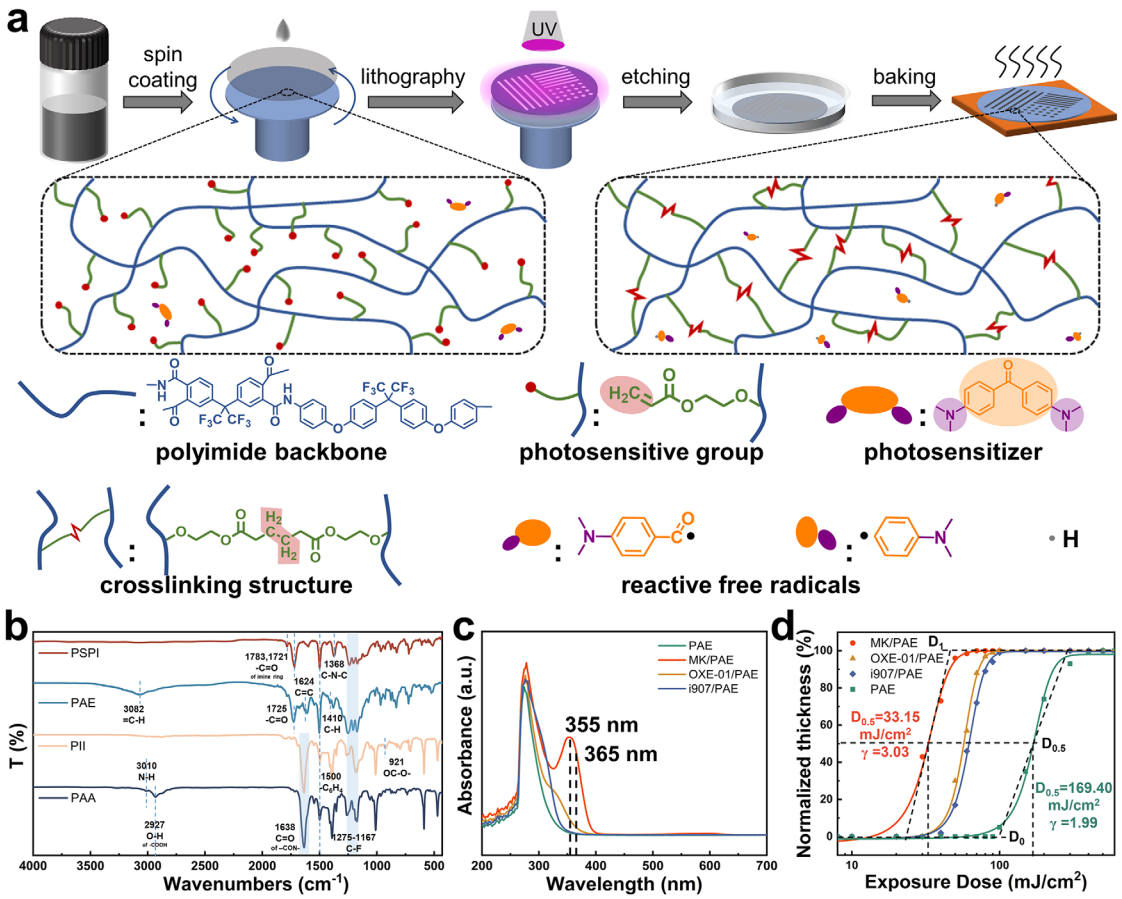

Figure 1. a) Schematic diagram of the photopatterning processes of PSPI and chemical changes after UV exposure. b) FTIR of PAA, PII, PAE (grafted HEA side chain) and PSPI (grafted HEA). c) UV–vis spectra of PAE solutions with various photo-initiators. d) Photosensitivity curves of MK/PAE, OXE-01/PAE, i907/PAE and PAE.

Figure S5, Supporting Information). Consequently, PAE exhibits excellent photocuring efficiency even at low photosensitizer concentrations (3 wt.%), and the MK/PAE formulation displays enhanced photosensitivity ($D_{0.5}$) of 33.15 mJ cm^{-2} and higher contrast (γ) of 3.03 compared to other PAE formulations (Figure 1d) and a fluorine-free MK/PAE system (Figure S6, Supporting Information).

2.2. Lithography Performance

The maximum resolution of the PSPI serves as a critical indicator of its capability to aid the fabrication of micro/nanoscale architectures. Photolithographic process parameters, including soft baking temperature and duration, UV exposure time, and development conditions, have a significant impact on the maximum resolution of photoresists and their derivatives.[25] Through the systematic photolithographic process optimization (detailed in Note S2 and Figure S7, Supporting Information), MK/PSPI achieves exemplary patterning fidelity when subjected to soft baking at 80 °C for 120 s, followed by 10 min of UV exposure and 7 s of development. MK/PAE (MK/PSPI precursor solution) exhibits superior photosensitivity, which suppresses thermal crosslinking during extended UV exposure, thus yielding patterns with higher contrast and sharper edges (**Figure 2**) than OXE-01/PAE or i907/PAE (Figure S8, Supporting Information).

Scanning electron microscopy (SEM) images (Figure 2d–f) reveal well-defined patterns with diverse profiles, smooth curve transitions, and distinct boundaries. No delamination or deformation is observed during development and rinsing, confirming strong adhesion between MK/PSPI and the silicon wafer. Furthermore, elemental analysis via energy-dispersive spectroscopy (EDS) confirms that Si is predominantly present in the unexposed regions, while the exposed areas exhibit the characteristic elemental composition of PSPI, as shown in Figure 2g–j and Figure S9 (Supporting Information). This distribution aligns precisely with the lithographic pattern, verifying the complete removal of unexposed PAE from the wafer surface. Contact aligner lithography (wavelength = 365 nm) using photomasks with 3 µm pitch line/space (L/S) patterns and 3 µm via arrays achieve feature dimensions of 3.2/2.8 µm (L/S) and hole diameters of ≈2.8 µm with excellent dimensional uniformity. Atomic force microscopy (AFM) analysis (Figure 2k,l) reveals that the crosslinked MK/PSPI exhibits trapezoidal architectures characterized by narrower top widths (2821 nm) and wider bases (≈3233 nm), with edge transition zones measuring more than

© 2025 Wiley-VCH GmbH

16163028, 0, Downloaded from https://advanced.onlinelibrary.wiley.com/doi/10.1002/adfm.202509278 by Zhiyuan Peng - East China Uni Of Sci & Tech , Wiley Online Library on [27/06/2025]. See the Terms and Conditions (https://onlinelibrary.wiley.com/terms-and-conditions) on Wiley Online Library for rules of use; OA articles are governed by the applicable Creative Commons License

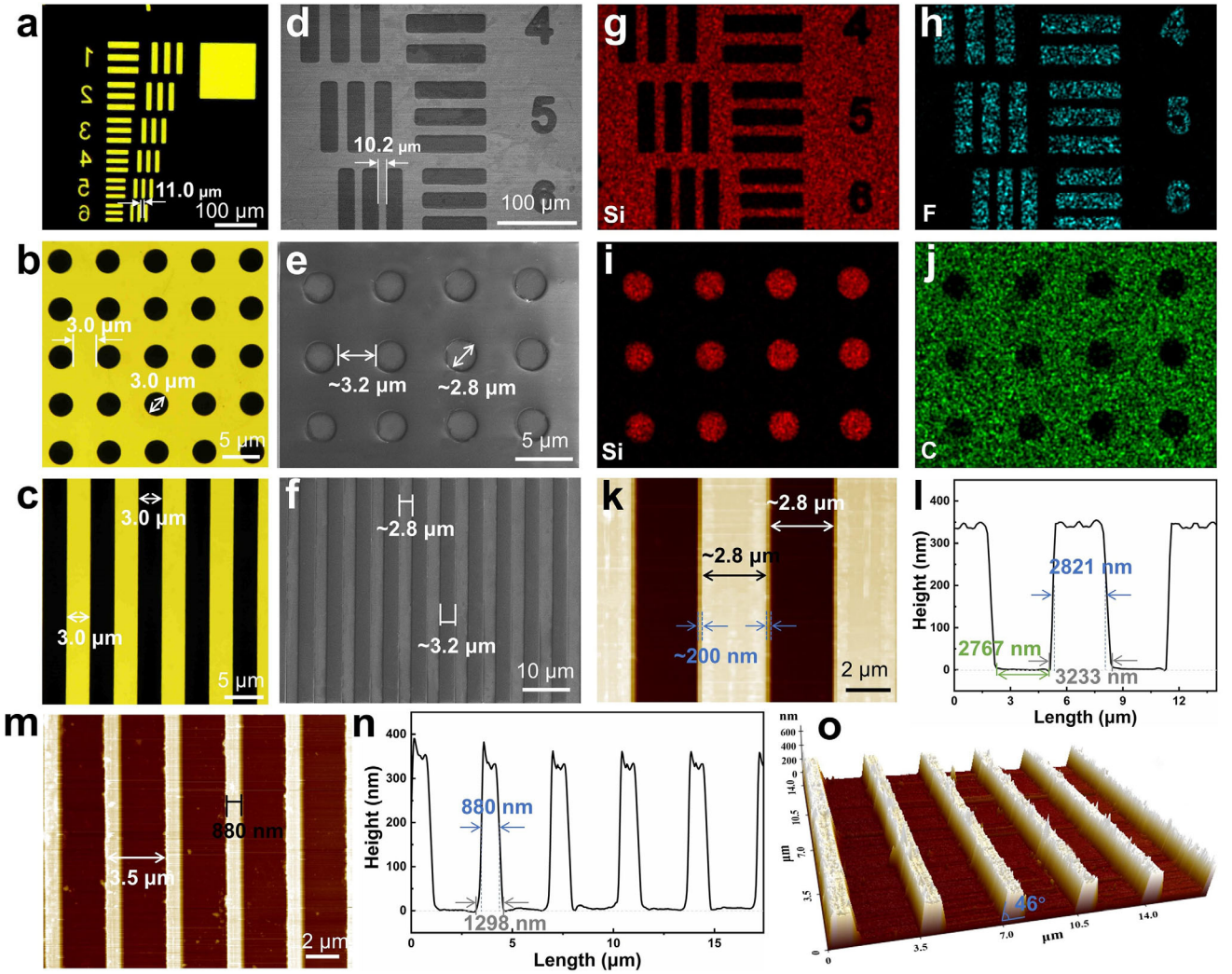

Figure 2. Optical microscope images of photomasks with a) complex, b) hole, and c) line patterns. SEM images of crosslinked MK/PSPI d) complex, e) hole, and f) line patterns. EDS spectrum of the g,i) Si, h) F, and j) C elements. k,m,o) AFM images of crosslinked MK/PSPI line patterns with different photomasks and l,n) the corresponding height differences.

200 nm in width. The average roughness (Ra) of the MK/PSPI surface is ≈8.039 nm shown in Figure S10 (Supporting Information). The dimensional discrepancies between the crosslinked MK/PSPI features and the original photomask geometry originate from Rayleigh and Mie scattering induced by the amorphous state or local chain ordering in elongated polymer structures,[26] which synergize with optical diffraction to broaden the effective exposure zone during photolithography. This is further compounded by anisotropic solubility in the developer solution during the wet etching process, resulting in the observed trapezoidal morphology.

To investigate the ultimate resolution capability of the MK/PSPI system, UV stepper lithography (wavelength = 365 nm) is employed. As illustrated in Figure 2m–o, MK/PSPI achieved a maximum resolution of 880 nm, with well-defined edges, high edge acuity, and a trapezoidal base angle of ≈46°. In addition, when employing high-precision through-hole photomasks with diameters of 600 nm, the upper PSPI layer exhibited clearly defined patterned features, whereas the lower layer demonstrated a pronounced loss in pattern fidelity, eventually leading to pattern disappearance, as shown in Figure S11 (Supporting Information). Nevertheless, based on its submicron lithographic resolution, the MK/PSPI formulation is successfully applied as a negative photoresist for fabricating the staggered electrode leads of nanomaterial-based field-effect transistors displayed in Figure S12 (Supporting Information). These findings underscore the capability of MK/PSPI to enable the fabrication of intricate, customized microstructures with high precision and reliability, pushing the maximum resolution of the PSPI to a submicron level.

2.3. Dielectric Properties and Comprehensive Performance

Both crosslinked PSPI and MK/PSPI exhibit enhanced tensile strength (104.7 and 102.5 MPa, respectively) compared to

© 2025 Wiley-VCH GmbH

16163028, 0, Downloaded from https://advanced.onlinelibrary.wiley.com/doi/10.1002/adfm.202509278 by Zhiyuan Peng - East China Uni Of Sci & Tech , Wiley Online Library on [27/06/2025]. See the Terms and Conditions (https://onlinelibrary.wiley.com/terms-and-conditions) on Wiley Online Library for rules of use; OA articles are governed by the applicable Creative Commons License

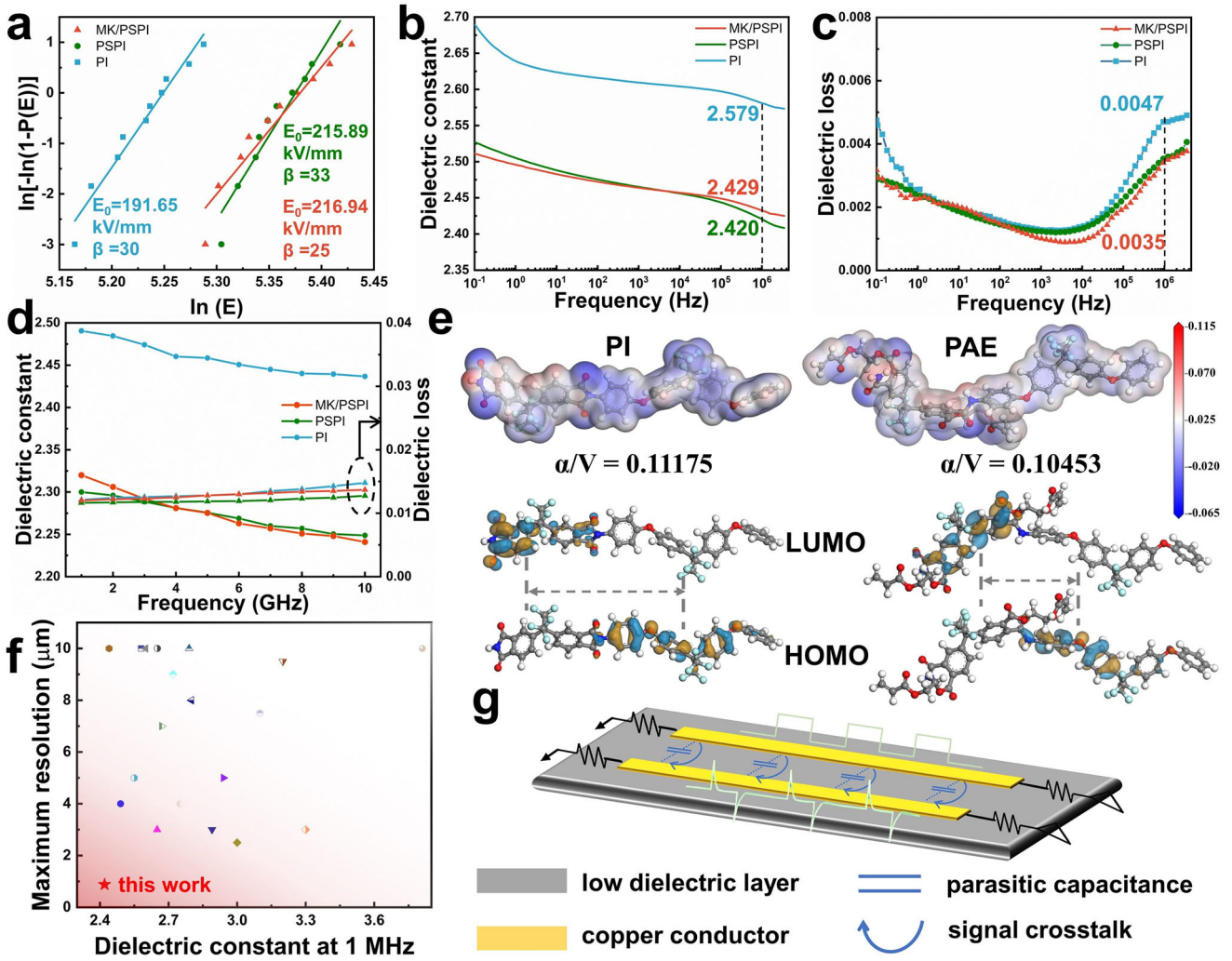

Figure 3. a) Weibull distribution, b) dielectric constant and c) dielectric loss with a frequency from 10^{-1} Hz to 4.3×10^6 Hz, and d) dielectric properties from 1 GHz to 10 GHz of MK/PSPI, PSPI and PI. e) Electrostatic potential maps and molecular orbitals of PI and PAE repeating unit. f) Comparison of dielectric constant and maximum resolution of low dielectric photosensitive materials. g) Signal crosstalk diagram.

ungrafted thermoplastic PI with the same backbone and maintain moderate elongation at break (≈11.6%), displayed in Figure S13 (Supporting Information). This improvement is attributed to the presence of ether bonds within the polymer backbone and side chains. Furthermore, the crosslinked networks of MK/PSPI and PSPI markedly improve their dimensional stability, yielding a low coefficient of thermal expansion (CTE) of ≈26.20 ppm K^{-1} from 20 to 180 °C (Figure S14, Supporting Information), thereby improving the compatibility with inorganic semiconductor or electrode materials. The initial thermal decomposition of MK/PSPI commences at 220 °C, with a 5 wt.% heat loss temperature ($T_{5\%}$) of 360 °C shown in Figure S15 (Supporting Information), ensuring a wide range of applications at high temperatures. The characteristic breakdown strength (E_0) and shape parameter (β) are calculated from the Weibull distribution in **Figure 3a**, where E_0 of MK/PSPI (216.94 kV mm^{-1}) is ≈13% higher than that of PI, indicating excellent dielectric breakdown strength and insulating properties. The crosslinked structure mitigates the adverse effects of thermal stress and partial discharge breakdown,[27] ensuring long-term operational stability under high voltage and current conditions. The highly similar X-ray diffraction patterns of PSPI and MK/PSPI (detailed in Figure S16 and Note S3, Supporting Information) indicate, demonstrating that the introduction of MK does not affect the network structure of PSPI. Overall, the incorporation of a small amount (3 wt.%) of the organic photosensitizer MK has a minimal impact on the overall performance of the PSPI system owing to negligible structural disruption.

The introduction of the low-polarization, flexible side chain HEA substantially reduces both the dielectric constant and dielectric loss ($\varepsilon = 2.420$, $\tan\delta = 0.0036$ at 1 MHz) of MK/PSPI to lower than those of PI ($\varepsilon = 2.579$, $\tan\delta = 0.0047$ at 1 MHz), as shown in Figure 3b,c, and also lower than those of the PSPI prepared with other photosensitive agents, as shown in Figure S17 (Supporting Information). The introduction of MK has a negligible impact on the dielectric properties. Due to the hydrophobicity of trifluoromethyl and the crosslinked structure of PSPI, MK/PSPI exhibits a water absorption rate of only 0.218% and maintains

© 2025 Wiley-VCH GmbH

16163028, 0, Downloaded from https://advanced.onlinelibrary.wiley.com/doi/10.1002/adfm.202509278 by Zhiyuan Peng - East China Uni Of Sci & Tech , Wiley Online Library on [27/06/2025]. See the Terms and Conditions (https://onlinelibrary.wiley.com/terms-and-conditions) on Wiley Online Library for rules of use; OA articles are governed by the applicable Creative Commons License

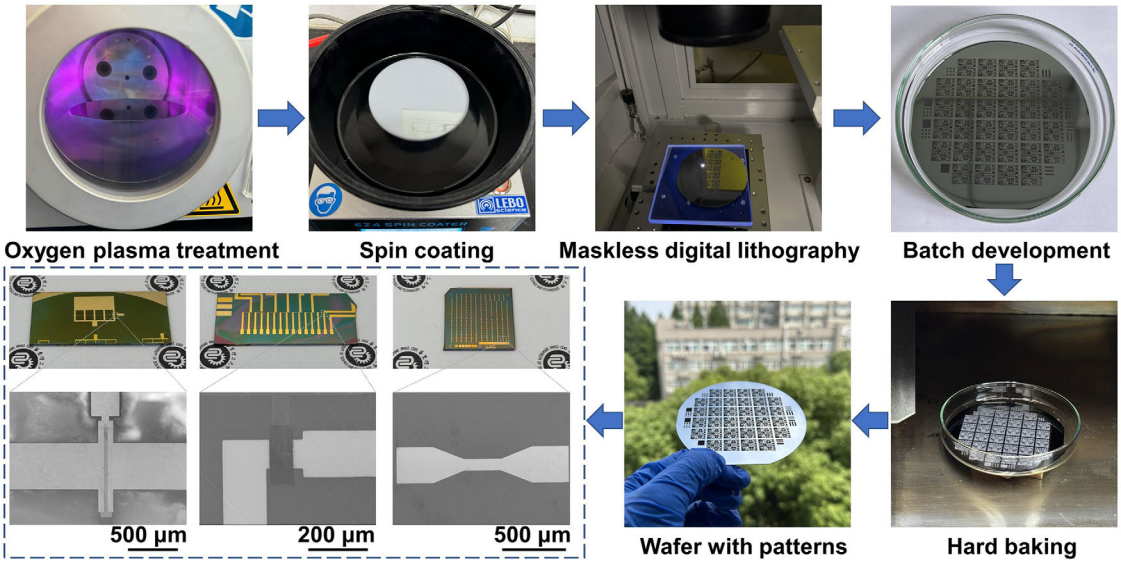

Figure 4. The LDW process of patterned MK/PSPI wafer using a photolithography machine and different patterns of field-effect transistors.

a stable dielectric constant after drying (Figure S18, Supporting Information). The increasing demand for high-frequency performance, especially in the context of advanced chip design and 5G communications, underscores the relevance of the dielectric behavior of MK/PSPI at GHz frequencies. At 10 GHz, MK/PSPI maintains a low dielectric constant of 2.241 and a dielectric loss of 0.0137 (Figure 3d), demonstrating its potential for stable signal transmission in high-frequency circuit boards. Electrostatic potential maps and molecular orbitals obtained through density functional theory (DFT) calculations (Figure 3e) reveal that the low-polarization flexible side chains with a larger molecular volume of PAE are rich in electronegative groups (-O-), effectively reducing the unit volume polarization and dipole moment. Additionally, the crosslinked structure of MK/PSPI restricts the movement of dipoles, further lowering the dielectric constant and hindering the rotation of matrix dipoles, ultimately reducing the intermolecular frictional work and dielectric loss. This material exhibits both a low dielectric constant and high resolution, outperforming other reported low-dielectric PSPI[16c,d,28] and photoresist polymers[29] (Figure 3f). These combined attributes enable reduced signal crosstalk in high-density integrated circuits (Figure 3g), ensuring the authenticity and integrity of signal transmission.

2.4. Maskless LDW and Quantum Sensor Applications

In addition to conventional photomask-based lithographic pattern preparation, MK/PSPI enables maskless LDW to create patterns owing to its high photosensitivity and contrast, eliminating the need for a photomask. The typical LDW process illustrated in **Figure 4** involves oxygen plasma treatment of cleaned wafers to increase surface wettability with the MK/PAE precursor solution, spin coating, and prebaking, followed by direct positioning on the lithography workstation. Complex patterns are designed using digital graphic drawing software (Figure S19, Supporting Information) and then inscribed onto the MK/PSPI film using a UV laser (wavelength = 355 nm), thereby circumventing the financial and temporal costs associated with photomask fabrication while significantly improving the productivity. Through the optimization of spot overlap, laser energy, and scanning speed, the patterns fabricated via LDW demonstrate topographically uniform surfaces and high-contrast edge profiles, achieving a maximum resolution of 27 μm and a Ra of 6.320 nm (Figure S20, Supporting Information), thereby enabling the precise fabrication of combinatorial architectures spanning micron-scale linear features to macroscale planar geometries. The exceptional thermal stability of MK/PSPI effectively mitigates localized decomposition and structural degradation induced by the high-power-density laser irradiation during LDW, thereby preserving the surface planarity of the irradiated regions. Subsequently, large-scale field-effect transistors with regular geometries and different patterns are fabricated by integrating physical vapor deposition and atomic layer deposition. This maskless lithography approach using MK/PSPI is not only fully compatible with conventional semiconductor processing on wafers but also offers a cost-effective and scalable solution for large-scale customization, thereby expanding its potential applications.

MK/PSPI serves as both a support substrate and a dielectric interlayer in multilayer flexible circuit boards fabricated via LDW, demonstrating excellent circuit encapsulation capabilities, as displayed in **Figures 5a** and S21,S22 (Supporting Information, the specific preparation procedures are detailed in the Supporting Information). Owing to its crosslinked network, lower curing temperature, excellent CTE matching with copper and polar groups of MK, the MK/PSPI exhibits a superior peel strength of 3.559 N cm^{-1} (Figure S23, Supporting Information). Also, the MK/PSPI-encapsulated circuit board exhibits fewer internal stress-induced defects and achieves more stable conductivity under repeated bending cycles compared to Kapton-based circuit boards (Figure 5b; Figure S24, Supporting Information). Time-domain spectra of the MK/PSPI circuit boards,

© 2025 Wiley-VCH GmbH

16163028, 0, Downloaded from https://advanced.onlinelibrary.wiley.com/doi/10.1002/adfm.202509278 by Zhiyuan Peng - East China Uni Of Sci & Tech , Wiley Online Library on [27/06/2025]. See the Terms and Conditions (https://onlinelibrary.wiley.com/terms-and-conditions) on Wiley Online Library for rules of use; OA articles are governed by the applicable Creative Commons License

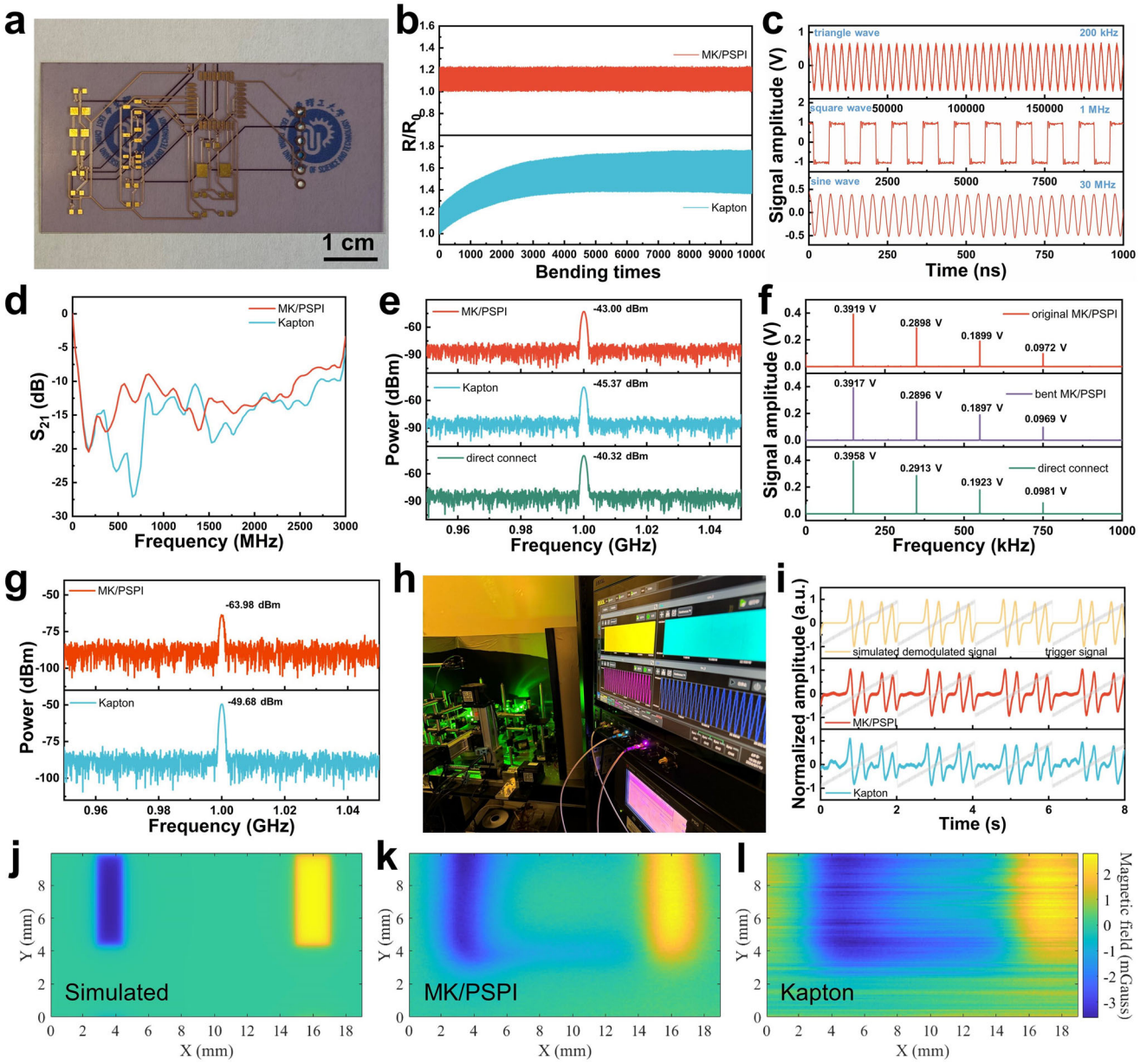

Figure 5. a) Multilayer MK/PSPI boards. b) Resistance changes with 10 000 bends of MK/PSPI and Kapton circuits. c) Time domain spectrum of signals with different waveforms transmitted by MK/PSPI circuit. d) S_{21} curves, e) signal power, and g) crosstalk power transmitted at 1 GHz of different substrate-based circuits and direct wire connection. f) Multi-frequency signal transmission before/after bending. h) Schematic diagram of the NV centers-magnetic sensor system. i) Demodulated signals obtained with MK/PSPI and Kapton circuit. j) theoretical magnetic field. Experimental magnetic field k) measured by the NV/MK/PSPI-based sensor, and l) measured by the NV/Kapton-based sensor.

produced by an arbitrary waveform generator (Agilent 33521A) with diverse amplitudes and waveforms (triangular waveforms at 200 kHz, square waveforms at 1 MHz, and sinusoidal waveforms at 30 MHz) confirm intact signal transmission, ensuring effective preservation of signal integrity in the low-dielectric MK/PSPI circuits (Figure 5c). In addition to signal integrity, the MK/PSPI circuit boards exhibit higher transmission efficiency (S_{21}), particularly between 400 MHz and 1 GHz, indicating superior transmission efficiency and reduced attenuation compared to their Kapton counterparts (Figure 5d). Further comparisons are made regarding the power attenuation during high-frequency signal transmission generated by a microwave generator (Windfreak Technologies SynthHD), as illustrated in Figure 5e and Figure S25 (Supporting Information). The MK/PSPI circuits attenuate the input signal (the direct connect power of −40.32 dBm) to −43.00 dBm at 1 GHz, which is less than the −45.37 dBm attenuation observed for Kapton boards, highlighting that the MK/PSPI substrates are more effective in reducing power loss for high-frequency signals. Compared to direct wire connections, the multifrequency signals

© 2025 Wiley-VCH GmbH

16163028, 0, Downloaded from https://advanced.onlinelibrary.wiley.com/doi/10.1002/adfm.202509278 by Zhiyuan Peng - East China Uni Of Sci & Tech , Wiley Online Library on [27/06/2025]. See the Terms and Conditions (https://onlinelibrary.wiley.com/terms-and-conditions) on Wiley Online Library for rules of use; OA articles are governed by the applicable Creative Commons License

transmitted through the initial MK/PSPI circuit (Figure 5f) exhibit an average amplitude retention of 99.08%, with an attenuation rate of only 0.13% after 10 000 bending cycles, indicating excellent durability and transmission stability. Moreover, MK/PSPI circuits exhibit significantly reduced crosstalk (−63.98 dBm) compared to Kapton-based circuits (−49.68 dBm) at 1 GHz (Figure 5g), with consistently lower crosstalk at other high frequencies (Figure S26, Supporting Information). Further S-parameter measurements (Figure S27, Supporting Information) confirm that MK/PSPI-based circuit boards exhibit lower crosstalk across a wide frequency range. These advantages arise primarily from the reduced parasitic capacitance and impedance mismatch of the low-dielectric MK/PSPI.

Given its superior signal transmission, MK/PSPI is considered for integration with nitrogen-vacancy (NV) centers in nanodiamonds to improve magnetic field measurement sensitivity. NV centers are known for their precision in detecting magnetic fields via Zeeman splitting.[30] Microwave signals are frequency-modulated to manipulate the NV centers, resulting in their acquisition of modulated magnetic field signals. This information is subsequently converted into electrical signals using a photodetector. However, these signals are often contaminated by noise, particularly electrical noise caused by crosstalk, parasitic capacitance, and impedance mismatch, thereby compromising their sensitivity and integrity.[31] Building on our previous work,[21,32] the low-dielectric NV/MK/PSPI-based sensor is employed to mitigate electrical noise during the transmission of modulated signals to a lock-in amplifier (Zurich Instruments HF2LI), where they are demodulated (as shown in Figure 5h). As shown in Figure 5i, the demodulated signals reveal that the NV/MK/PSPI-based sensor outperforms the NV/Kapton-based sensor, delivering more stable waveforms with improved signal clarity. Consequently, the NV/MK/PSPI-based sensor can transmit frequency-modulated signals, demonstrating its suitability for practical use and its ability to provide accurate data for precision sensing. Both the NV/MK/PSPI-based and NV/Kapton-based sensors are applied to measure the magnetic field generated by current-carrying wires (Figure S28, Supporting Information). The NV/MK/PSPI-based sensor (Figure 5k) exhibits superior performance, delivering magnetic field images with greater clarity and capturing finer details that closely align with the theoretical distribution (Figure 5j) compared to the NV/Kapton-based sensor (Figure 5l). Comparisons of additional magnetic field tests for the current-carrying wires are detailed in Figure S29 (Supporting Information). Notably, accurate magnetic field imaging is achieved even at weak magnetic field strengths (≈mGauss),[33] highlighting the sensor's capability to operate effectively under such conditions. This is because the MK/PSPI-integrated NV magnetometer achieves magnetic field sensitivity at the nanotesla (nT)/$Hz^{1/2}$ level, as demonstrated by the spectral response shown in Figure S30 (Supporting Information). The sensitivity exhibits a characteristic 1/f noise dependence, with significantly enhanced performance at higher frequencies, where the reduced noise floor enables sub-nT/$Hz^{1/2}$ resolution. This sensitivity stems from the exceptionally low dielectric loss and minimized crosstalk in the MK/PSPI substrate. These enable precise weak-field measurements, including faint magnetic imaging and biomagnetic detection, while offering unprecedented flexibility for integration with miniaturized quantum sensing platforms.

3. Conclusion

An innovative photosensitive polyimide system that combines chemical amplification with intrinsic low-polarization photosensitive groups has been designed to effectively address the long-standing challenge of achieving both high resolution and a low dielectric constant. Our study demonstrates an electronic material with exceptional dielectric properties (ε = 2.241, tanδ = 0.0137 at 10 GHz), ultrahigh-resolution (≈880 nm), and excellent photosensitivity (33.15 mJ cm^{-2}). Among the systems tested, the MK/PSPI(HEA-grafted) system allows for efficient large-scale pattern customization via both photomask and maskless lithography, facilitating the fabrication of field-effect transistors and flexible multilayer circuit boards. The robustness and efficiency of MK/PSPI in signal transmission outperform those of conventional dielectric materials such as Kapton, with improved resistance stability under repeated bending, enhanced signal precision, and low crosstalk at high frequencies. Furthermore, NV centers in diamond integrated with low-dielectric MK/PSPI circuit boards exhibit strong potential for precision quantum sensing, achieving magnetic field sensitivity at the nanotesla (nT/$Hz^{1/2}$) level. Collectively, the MK/PSPI system represents a significant advancement in next-generation electronic materials, offering wide applicability in integrated circuits and high-fidelity signal transmission technologies.

4. Experimental Section

Synthesis of PSPI and Exploration of Lithography Processes: A 15 wt.% solution of polyamide ester (PAE) precursor with a moderate molecular weight (Mn = 18 kDa) was prepared by 11 mmol (6.3960 g) of diamine 6FBAPP and 10 mmol (4.442 g) of dianhydride 6FDA in DMAc under N_2, stirring overnight at room temperature; 45 mmol of trifluoroacetic anhydride (TFAA, 9.45135 g) and 45 mmol of triethylamine (TEA, 4.55355 g) were then added dropwise at 0 °C and stirred for 24 h, followed by addition of 100 mmol of the desired photosensitive monomer (HEMA, HPMA, HEA, or HPA) and stirring at 52 °C for 24 h. The reaction mixture was precipitated into deionized water under vigorous stirring, the fibrous solid was filtered, extracted through a 0.8 µm membrane, washed repeatedly with isopropanol (IPA) and water, and vacuum-dried at 40 °C for 24 h to yield PAE. For patterning, 1 g PAE and 0.0309 g photoinitiator (MK, OXE-01, or i907) were dissolved in 2.4 g DMAc, spin-coated onto cleaned Si wafers (1000–6000 rpm), prebaked, UV-exposed through a mask at 365 nm, developed in cyclopentanone to remove uncured regions, and finally thermally imidized at 180 °C for 2 h to obtain PSPI micropatterns. The synthesis process of precursor PAE and chemical changes after UV exposure are shown in Scheme S1 (Supporting Information).

Synthesis of Conventional Polyimide (PI): The PI (6FDA-6FBAPP) was employed as a performance control for PSPI. A 15 wt.% PAA solution was prepared by adding equimolar 6FBAPP and 6FDA under N_2. After combing, the mixture was moved to room temperature and stirred for 22 h to synthesize PAA. This solution was cast onto a clean glass plate and thermally imidized as follows: hold at 60 °C for 2 h; ramp at 1 °C min^{-1} to 80, 120, 160, and 200 °C, holding 40 min at each temperature; then ramp at 2 °C min^{-1} to 270 °C and hold for 1.5 h to produce the PI (6FDA–6FBAPP) film.

Maskless Lithography for Patterned PSPI: A silicon wafer with clean surfaces was primed in an oxygen plasma processor for 30 s in order to increase the contact angle between the precursor solution and the wafer. The precursor solution was deposited onto the wafer via spin coating at 600 rpm, followed by acceleration to a speed of 3000 rpm for 30 s. The wafer was pre-baked in an 80 °C oven for 120 s. It was then placed directly

© 2025 Wiley-VCH GmbH

16163028, 0, Downloaded from https://advanced.onlinelibrary.wiley.com/doi/10.1002/adfm.202509278 by Zhiyuan Peng - East China Uni Of Sci & Tech , Wiley Online Library on [27/06/2025]. See the Terms and Conditions (https://onlinelibrary.wiley.com/terms-and-conditions) on Wiley Online Library for rules of use; OA articles are governed by the applicable Creative Commons License

on the workbench underneath the photolithography laser machine. The patterns on the software (Ezcad2) were photolithographed directly onto the wafer, circumventing the use of a mask plate, at a speed of 50 mm s^{-1}, with 10% power, 30 kHz, and a total of 5 passes. Subsequently, the wafer was immersed in a cyclopentanone solution and shaken for 7 s, used a nitrogen blow gun to blow dry the surface liquid and transferred to an oven at 180 °C for a 2-h drying period. The large-scale patterned silicon wafer was ultimately produced.

Simulations Section: The molecular structures of PI (6FDA-6FBAPP) and PAE were established by Material Studio (Accelrys, Inc.). The density functional theory (DFT) simulation calculation was performed by B3LYP (Becke's three-parameter nonlocal exchange and Lee–Yang–Parr's correlation) functional in the DMol3 module for geometry optimization using the grimme method for DFT-D correction, in which core treatment is all electron, the SCF tolerance was 1×10^{-6}, DIIS size was 6 and smearing was 0.005 Ha. The polarizability and dipole moment of the repeating unit after structural optimization were calculated using the VAMP module. The mean square displacement and diffusion coefficient were calculated using molecular dynamics simulations, and the specific model establishment, equilibrium process, and calculation methods were described in our previous article.[21]

Supporting Information

Supporting Information is available from the Wiley Online Library or from the author.

Acknowledgements

Z.P. and A.Y. contributed equally to the work. The authors are grateful to Prof. Yuhang Li from the School of Materials Science and Engineering at East China University of Science and Technology for his guidance on the structure and language of the manuscript. The authors would like to thank Prof. Pooi See Lee's team at Nanyang Technological University for their help and suggestions during the revision. This work was supported by the National Natural Science Foundation of China (22278140, U22B20143) and the Science and Technology Commission of Shanghai Municipality (22DZ1205900). This project was supported by the Shanghai Municipal Science and Technology Major Project and the Fundamental Research Funds for Central Universities.

Conflict of Interest

The authors declare no conflict of interest.

Data Availability Statement

The data that support the findings of this study are available from the corresponding author upon reasonable request.

Keywords

high photosensitivity, high resolution, laser direct writing, low dielectric constant, photosensitive polyimide, quantum sensing

Received: April 13, 2025
Revised: June 2, 2025
Published online:

[1] a) D. Zhong, C. Wu, Y. Jiang, Y. Yuan, M.-g. Kim, Y. Nishio, C.-C. Shih, W. Wang, J.-C. Lai, X. Ji, T. Z. Gao, Y.-X. Wang, C. Xu, Y. Zheng, Z. Yu, H. Gong, N. Matsuhisa, C. Zhao, Y. Lei, D. Liu, S. Zhang, Y. Ochiai, S. Liu, S. Wei, J. B. H. Tok, Z. Bao, *Nature* **2024**, *627*, 313; b) L. Wang, Z. Yi, Y. Zhao, Y. Liu, S. Wang, *Chem. Soc. Rev.* **2023**, *52*, 795.
[2] K.-i. Fukukawa, M. Ueda, *Polym. J.* **2008**, *40*, 281.
[3] S. H. Pyo, M. Y. Lee, J. J. Jeon, J. H. Lee, M. H. Yi, J. S. Kim, *Adv. Funct. Mater.* **2005**, *15*, 619.
[4] R. Zhu, H. Liang, S. Liu, Y. Yuan, X. Wang, F. C.-C. Ling, A. Kuznetsov, G. Zhang, Z. Mei, *Nat. Commun.* **2023**, *14*, 5396.
[5] Y. Shin, Y. W. Kim, H. J. Kang, J. H. Lee, J. E. Byun, J.-Y. Yang, J. W. Lee, *Nano Lett.* **2023**, *23*, 5391.
[6] a) D.-J. Liaw, K.-L. Wang, Y.-C. Huang, K.-R. Lee, J.-Y. Lai, C.-S. Ha, *Prog. Polym. Sci.* **2012**, *37*, 907; b) Y. C. Huang, H. W. Hu, Y. H. Liu, H. C. Hsieh, K. N. Chen, *IEEE J. Electron Devices Soc.* **2024**, *12*, 96.
[7] D. Jayachandran, R. Pendurthi, M. U. K. Sadaf, N. U. Sakib, A. Pannone, C. Chen, Y. Han, N. Trainor, S. Kumari, T. V. Mc Knight, J. M. Redwing, Y. Yang, S. Das, *Nature* **2024**, *625*, 276.
[8] X. Dong, B. Wan, J.-W. Zha, *Chem. Rev.* **2024**, *124*, 7674.
[9] O. Vazquez-Mena, T. Sannomiya, M. Tosun, L. G. Villanueva, V. Savu, J. Voros, J. Brugger, *ACS Nano* **2012**, *6*, 5474.
[10] W. Cao, H. Bu, M. Vinet, M. Cao, S. Takagi, S. Hwang, T. Ghani, K. Banerjee, *Nature* **2023**, *620*, 501.
[11] M.-H. Chen, C.-C. Lai, H.-L. Chen, Y.-H. Lin, K.-Y. Huang, C.-H. Lin, H.-T. Hsiao, L.-C. Liu, C.-M. Chen, *Mater. Sci. Semicond. Process.* **2018**, *88*, 132.
[12] S. Choi, S. Lee, J. Jeon, J. An, S. B. Khan, S. Lee, J. Seo, H. Han, *J. Appl. Polym. Sci.* **2010**, *117*, 2937.
[13] L.-Y. Tseng, Y.-C. Lin, C.-C. Kuo, C.-C. Kuo, M. Ueda, W.-C. Chen, *React. Funct. Polym.* **2020**, *157*, 104760.
[14] a) Z. Ma, T. Li, X. Dai, X. Shen, X. Wang, H. Fu, X. Xia, Q. Zhu, Y. Zhu, Z. Yu, C. Cao, S. You, C. Kuang, *Adv. Funct. Mater.* **2024**, *34*, 2409859; b) Q. Lin, *Polymer* **2023**, *286*, 126395.
[15] M. Zhang, S. Jiang, Y. Gao, J. Nie, F. Sun, *Chem. Eng. J.* **2020**, *390*, 124625.
[16] a) H. Meng, K. Chen, C. Li, Y. He, Z. Huang, H. Huang, Z. Chi, S. Liu, Y. Zhang, *ACS Appl. Polym. Mater* **2025**, *7*, 3815; b) P. Zhang, H. Wang, P. Xia, X. Chen, W. Zhao, C. Wang, X. Meng, B. Jia, *Polymers* **2024**, *16*, 1805. c) S. Huang, X. Lv, X. Lai, J. Li, Y. Zhang, S. Qiu, G. Zhang, R. Sun, *Chem. Eng. J.* **2023**, *477*, 146858; d) X. Lai, J. Zhang, Z. Yang, S. Huang, J. Li, G. Zhang, R. Sun, *Mater. Today Commun.* **2023**, *37*, 107316.
[17] a) O. Norimasa, T. Chiba, M. Hase, T. Komori, M. Takashiri, *J. Alloys Compd.* **2022**, *898*, 162889; b) W. Chen, S. Liu, Y. Sun, X. Zhou, F. Zhou, *Macromol. Mater. Eng.* **2022**, *307*, 2100645.
[18] a) N. Nasir, S. Kumar, M. Kim, V. H. Nguyen, M. Suleman, H. M. Park, S. Lee, D. Kang, Y. Seo, *ACS Appl. Energy Mater.* **2022**, *5*, 6986; b) C. Jin, C. Feng, Y. Chen, T. Zhang, H. He, H. Na, J. Zhu, *Energy Environ. Sci.* **2024**, *17*, 5931.
[19] W. Chen, W. Chen, B. Zhang, S. Yang, C.-Y. Liu, *Polymer* **2017**, *109*, 205.
[20] X. Liu, J. Zhou, Y. Zhou, M. Wu, Y. Zhu, J. Zhao, S. Liu, H. Xiao, *Eur. Polym. J.* **2022**, *173*, 111315.
[21] Z. Peng, A. Ye, L. Zhang, X. Li, C. Lian, C. Li, *Compos. Commun.* **2024**, *46*, 101804.
[22] P. Garra, J. P. Fouassier, S. Lakhdar, Y. Yagci, J. Lalevée, *Prog. Polym. Sci.* **2020**, *107*, 101277.
[23] H. Hou, J. Jiang, M. Ding, *Eur. Polym. J.* **1999**, *35*, 1993.
[24] a) T. Fukushima, T. Oyama, M. Tomoi, *React. Funct. Polym.* **2003**, *56*, 59; b) S. Dadashi-Silab, C. Aydogan, Y. Yagci, *Polym. Chem.* **2015**, *6*, 6595.
[25] X.-Y. Lu, R.-S. Zhang, G.-W. Yang, Q. Li, B. Li, G.-P. Wu, *Angew. Chem., Int. Ed.* **2024**, *63*, 202401850.

© 2025 Wiley-VCH GmbH

16163028, 0, Downloaded from https://advanced.onlinelibrary.wiley.com/doi/10.1002/adfm.202509278 by Zhiyuan Peng - East China Uni Of Sci & Tech , Wiley Online Library on [27/06/2025]. See the Terms and Conditions (https://onlinelibrary.wiley.com/terms-and-conditions) on Wiley Online Library for rules of use; OA articles are governed by the applicable Creative Commons License

[26] Y. Zhang, H. Yu, L. Wang, X. Wu, J. He, W. Huang, C. Ouyang, D. Chen, B. E. Keshta, *Adv. Colloid Interface Sci.* **2024**, *329*, 103197.

[27] X.-J. Liu, M.-S. Zheng, G. Chen, Z.-M. Dang, J.-W. Zha, *Energy Environ. Sci.* **2022**, *15*, 56.

[28] a) L.-Y. Tseng, Y.-C. Lin, C.-C. Kuo, C.-K. Chen, C.-E. Wang, C.-C. Kuo, M. Ueda, W.-C. Chen, *J. Polym. Sci.* **2020**, *58*, 2366; b) J.-x. Ma, L.-l. Yuan, S.-n. Fan, L.-z. Wang, B. Jia, H.-x. Yang, S.-y. Yang, *Eur. Polym. J.* **2023**, *192*, 112071; c) T. Wang, J. Zhang, J. Li, X. Lv, L. Shan, G. Zhang, R. Sun, C.-P. Wong, *Compos. Commun.* **2023**, *38*, 101469; d) S. Srisuwan, S. Thongyai, P. Praserthdam, *J. Appl. Polym. Sci.* **2010**, *117*, 2422; e) A. R. Dick, W. K. Bell, B. Luke, E. Maines, B. Mueller, B. Rawlings, P. A. Kohl, C. G. Willson, *J. Micro-Nanolithogr. Mems Moems* **2016**, *15*, 033503; f) K. Kikuchi, S. Segawa, E. S. Jung, Y. Nemoto, M. Umemoto, H. Nakagawa, K. Tokoro, M. Aoyagi, *Jpn. J. Appl. Phys. Part 1* **2004**, *43*, 4141; g) H. Seino, O. Haba, M. Ueda, A. Mochizuki, *Polymer* **1999**, *40*, 551; h) T. Miyagawa, T. Fukushima, T. Oyama, T. Iijima, M. Tomoi, *J. Polym. Sci. Part A-Polym. Chem.* **2003**, *41*, 861; i) Y. Watanabe, Y. Shibasaki, S. Ando, M. Ueda, *Chem. Mater.* **2002**, *14*, 1762; j) B. Fan, M. Zhou, C. Zhang, D. He, J. Bai, *Prog. Polym. Sci.* **2019**, *97*, 101143; k) Y. Watanabe, Y. Shibasaki, S. Ando, M. Ueda, *Polym. J.* **2005**, *37*, 270; l) M. Hasegawa, A. Tominaga, *J. Photopolym. Sci. Technol.* **2005**, *18*, 307.

[29] a) H. Du, Y. Deng, X. Hu, J. Peng, H. Hu, Y. Tang, X. Ye, J. Ma, J. Yang, *React. Funct. Polym.* **2024**, *200*, 105935; b) H. Zhu, Y. Su, J. Li, Y. Ding, M. Li, W. Li, *ACS Appl. Polym. Mater* **2024**, *6*, 6130; c) S.-S. Lin, Y.-J. Chan, Y.-D. Lee, *J. Appl. Polym. Sci.* **2013**, *127*, 3269; d) Q. Long, X. Li, Y. Huang, Q. Peng, X. Li, L. Zhu, J. Ma, X. Ye, J. Yang, *J. Appl. Polym. Sci.* **2022**, *139*, 52614; e) J. Peng, Q. Peng, L. Fan, X. Li, J. Ma, J. Yang, *RSC Adv.* **2025**, *15*, 7956.

[30] J. F. Barry, J. M. Schloss, E. Bauch, M. J. Turner, C. A. Hart, L. M. Pham, R. L. Walsworth, *Rev. Mod. Phys.* **2020**, *92*, 015004.

[31] a) J. F. Barry, M. J. Turner, J. M. Schloss, D. R. Glenn, Y. Song, M. D. Lukin, H. Park, R. L. Walsworth, *Proc. Natl. Acad. Sci. USA* **2016**, *113*, 14133; b) T. Wolf, P. Neumann, K. Nakamura, H. Sumiya, T. Ohshima, J. Isoya, J. Wrachtrup, S. D. Magnetometry, *Phys. Rev. X* **2015**, *5*, 041001.

[32] A. Ye, D. Fu, M. Wu, J. Guo, T. Sheng, X. Li, S. Gong, Y. Niu, *Chin. Opt. Lett.* **2023**, *21*, 111201.

[33] a) D. L. Sage, K. Arai, D. R. Glenn, S. J. DeVience, L. M. Pham, L. Rahn-Lee, M. D. Lukin, A. Yacoby, A. Komeili, R. L. Walsworth, *Nature* **2013**, *496*, 486; b) S. Chen, W. Li, X. Zheng, P. Yu, P. Wang, Z. Sun, Y. Xu, D. Jiao, X. Ye, M. Cai, M. Shen, M. Wang, Q. Zhang, F. Kong, Y. Wang, J. He, H. Wei, F. Shi, J. Du, *Proc. Natl. Acad. Sci.* **2022**, *119*, 2118876119; c) N. Mosavian, F. Hubert, J. Smits, P. Kehayias, Y. Silani, B. A. Richards, V. M. Acosta, *ACS Nano* **2024**, *18*, 6523.

© 2025 Wiley-VCH GmbH

16163028, 0, Downloaded from https://advanced.onlinelibrary.wiley.com/doi/10.1002/adfm.202509278 by Zhiyuan Peng - East China Uni Of Sci & Tech , Wiley Online Library on [27/06/2025]. See the Terms and Conditions (https://onlinelibrary.wiley.com/terms-and-conditions) on Wiley Online Library for rules of use; OA articles are governed by the applicable Creative Commons License